Journal Européen des Systèmes Automatisés
Vol. 59, No. 7, July, 2026, pp. 2095-2110
Journal homepage: http://iieta.org/journals/jesa

Biomechanical Evaluation of a Ti-6Al-4V Intramedullary Nail Fixation for Subtrochanteric Femur Fractures under Physiologic Gait Loads

Haneen Mahdi Jaber[1*], Ali Taha Mohammed[2], Ahmed Hashim Kareem[3], Marwah Ali Harb[3], Diana Abd Alkareem Noori Kattab[4], Ameen M. Al-Juboori[5]

[1] Department of Mechanical Technologies, Technical Institute – Suwaira, Middle Technical University, Suwaira 52002, Iraq
[2] Mechanical Techniques Department, Amarah Technical Institute, Southern University, Basra 62001, Iraq
[3] Mechanical Techniques Department, Amarah Technical Institute, Southern Technical University, Basra 62001, Iraq
[4] Metallurgy and Production Engineering College, University of Technology, Baghdad 10066, Iraq
[5] Mechanical Power Techniques Engineering Department, Technical Engineering College, Al-Mustaqbal University, Hillah 51001, Iraq

Corresponding Author Email: haneed-mahdi@mtu.edu.iq

https://doi.org/10.18280/jesa.590724

Received: 12 May 2026
Revised: 14 July 2026
Accepted: 21 July 2026
Available online: 31 July 2026

Keywords:
subtrochanteric fracture, intramedullary nail, gait loading, locking screws, cortical stress

ABSTRACT

An 80 kg adult femur three-dimensional finite element model with a subtrochanteric fracture was developed, in which the fracture was stabilized with a Ti-6Al-4V intramedullary nail and four locking screws, and the construct mechanics were quantified under standing, walking, and running loads estimated from gait data. A hex-symmetric 0.6 mm tetrahedral mesh ensured that predictions of deformation and von Mises stress were independent of the mesh. A vertical hip contact force of 784.8 N (standing), 784–1150 N (walking), and 1962–2353 N (running) with an anteroposterior component of 120–196 N and a mediolateral component of 39–80 N was applied to the nail and partitioned to the screws. Maximum total deformation increased non-linearly from 0.74 mm in the standing case to 1.98 and 2.95 mm in the walking cases and 3.59 and 2.95 mm in the running cases, with maximum peaks all situated at the femoral head, demonstrating a switch from column-like (standing) to cantilever-like (walking and running cases) behaviour. During standing, interfragmentary micromotion at the subtrochanteric gap remained below ~0.3 mm; it fell within the sub-mm range during walking and reached a few mm-equivalent head motion during running, indicating that walking is a more appropriate stimulus for secondary callus. Implant stresses in the Ti-6Al-4V nail and screws were far below yield: <50 MPa during standing, maximums of 80.7 and 206 MPa during walking, and total shaft stresses largely <70 MPa during running, all of which were at ≤24% of the 845.7 MPa yield strength. By comparison, at the distal screw–entry cortex, cortical bone experienced immediately following standing, walking, and running cases were 61.7 MPa (standing), 206 MPa (walking), and 291–292 MPa (running), made the distal screw-cortex interface the most susceptible fatigue damage site, and gave a preliminary biomechanical interpretation for future design optimization as well as clinical evaluation of rehab protocols for reduction of the distal cortical stress concentration.

1. INTRODUCTION

Finite element analysis (FEA) has therefore become an essential tool for exploring the complex biomechanics of lower limb fracture fixation and optimising local implants, in a way that is difficult to replicate in an experimental setting. Throughout the literature review, progressively subject-specific models that include direct computed tomography (CT)-specific density mapping, neuromusculoskeletal-generated gait loading, and implant–bone contact details are used to predict stresses, strains, micromotion, and healing-relevant stimuli. Tucker et al. [1] used the active complex of a parametric finite element model of nine types of AO/OTA proximal femoral fractures fixed with intramedullary nails during heel-strike gait in a subject weighing 85.7 kg to study biomechanics. They systematically varied nail diameter, length, material, and distal locking screws while accounting for muscle forces and frictional contact between bone, nail, and screws. Ye et al. [2] investigated the impact of proximal trabecular bone CT values on stress distribution and stability in an intertrochanteric model fixed with a proximal femoral nail antirotation (PFNA) device and created a finite element model. Lowen et al. [3] conducted a parametric f FEA of a mouse transverse femoral osteotomy stabilized with a locked intramedullary nail. Identification of design parameters that significantly influence interfragmentary strain (IFS). Employing a murine femur based on micro-CT, they modified nail material (stainless steel vs. Polyether ether ketone), nail–bone clearance, interlocking screw spacing, and, for additional runs, nail diameter, under combined axial and bending loads simulating peak gait forces. Yang et al. [4] employed CT-based density to map finite element models of Seinsheimer type IIIA and V subtrochanteric fractures, and created models of proximal femoral bionic nail (PFBN) and three conventional long intramedullary nails (InterTAN, PFNA, RCN) to compare them under axial, bending, and torsional load. Fu et al. [5] reported that anterior cortical bone loss after screw fixation of aggressive benign femoral neck lesions may predispose to subsequent fracture-dislocation. Combined cadaveric testing and CT-based FEA to assess two 6.5 mm cannulated screws as prophylactic fixation for aggressive benign femoral neck lesions with up to 50% anterior cortical bone loss. Hidaka et al. [6] retrospectively evaluated 133 hips after CT-navigated total hip arthroplasty to identify postoperative combined anteversion (CA) ranges that provide an impingement-free prosthetic range of motion by Yoshimine's criteria. Wang et al. [7] combined CT-based FEA with artificial-bone mechanical evaluation to compare standard AO cannulated screw placement versus 15° posterior-tilt screws for Pauwels Type 3 femoral neck 70 fractures with 15° posterior tilt. Kishore et al. [8] followed 39 distal femoral fractures treated with retrograde intramedullary nailing in a prospective study. They reported good or excellent functional results in about 95% of patients, a union rate of 94.9% with only one case of non-union and one delayed union, and no infections or hardware failures. Trompeter et al. [9] investigated how to protect distal screws in comminuted distal femur constructs mechanically. Xu et al. [10] developed a validated finite element model of a laterally based distal femoral locking plate spanning a 45 mm metaphyseal defect. Adding oblique kickstand screws reduced the maximum plate stress near the fracture by about 40%, lowered metaphyseal screw stresses by up to one-third, and decreased forces at the locking screw-plate interface by about 20-23%. Martínez-Martínez et al. [11] developed a patient-specific in-silico framework to couple a Cartesian grid finite element method with a fuzzy-logic callus healing model for simulating long-bone fracture healing under individualized gait loads, comparing stainless steel, titanium, magnesium, and polylactic acid (PLA) nails. Bavil et al. [12] conducted a randomized clinical finite-element study involving 16 middle-aged and elderly patients with complex tibial plateau fractures. This showed that finite element-based preoperative planning with dual-plate fixation substantially reduced operative time, internal fixation costs, and total hospitalisation expenses. Bavil et al. [13] used a strength model based on a combined patient-specific neuromusculoskeletal modelling and FEA in three paediatric proximal femoral osteotomy cases, studying how different neck-shaft and anteversion angles affected bone–implant micromotion and implant peak von Mises stress. Ülker et al. [14], using a similar finite element framework informed by the neuromusculoskeletal response of bone and soft tissue, one previous study paired six paediatric PFO patients with four blade plate width-to-neck-diameter ratios (30–60%) to evaluate the effects on implant yield risk and factors of safety, and showed that larger ratios reduced yield risk and increased factor of safety. Eghan-Acquah et al. [15] optimized a new patellar fixation implant using finite element design principles and performed biomechanical comparisons versus classic tension band wiring in 20 calf patellae, finding significantly higher failure loads (≈1130 vs 681 N) and less fracture-line width with the new device, suggesting improved stability and potential reduction of hardware-burden complications.

Most analyses of these finite elements used to evaluate subtrochanteric intramedullary fixation have focused on a single load, usually a single-leg stance or a single force from one daily activity, and most analyses of the constructs have been in the context of the peak force in the implant. Three questions therefore remain that have not been fully answered: (i) how the load transfer behavior in a locked nail construct changes qualitatively as a function of physiologic activity from quiet standing to running, including how shear reversal during gait-phases affects the behavior; (ii) whether the load transfer behavior of a Ti-6Al-4V construct or the surrounding cortical bone is the mechanically limiting factor, as a function of physiologic activity; and (iii) how the load transfer behavior of a Ti-6Al-4V construct as a function of physiologic activity maps onto a practical staged rehabilitation timeline. The aims of the present study were to fill this gap by applying a graded standing–walking–running load spectrum, using fully decomposed three-dimensional hip contact forces, and by studying it in a single subtrochanteric construct. Main findings of this work are: (1) Description of a column-to-beam-to-cantilever transition in construct behavior over the course of the activity spectrum and identification of the components of force that govern each of these regimes: (2) Demonstration that the Ti-6Al-4V nail and screws are far from yield (≤24%) under all conditions, so that the distal screw–cortex interface, not the implant, is the critical site for fatigue and failure: (3) Translation of the predicted micromotion into a weight-bearing and rehabilitation schedule based on the activity.

2. SIMULATION MODEL MATERIALS

The material properties of the bone elements were assigned using data from earlier research papers [16, 17]. Cortical bone from the femoral diaphysis has an average longitudinal Young's modulus; dynamic measurement gives a value of ~19.9 GPa. There is a strong correlation between modulus and apparent density (as per relations such as):

$$E = 2065\rho^{2.89} \text{ GPa axially} \quad (1)$$

Young modulus of trabecular bone in the proximal femur is low (average 11.4 GPa) due to its porous structure, or perhaps is approximately 1 GPa for proximal regions in some models. Varying with density, the values range from 6.9 to 14 GPa, depending on the area and the donor's age. Apparent density relationships include

$$E = 1904\rho^{1.64} \text{ GPa axially} \quad (2)$$

For normal adults, the bone density in the femur normally varies between 1 and 1.2 g/cm³, depending on anatomic and demographic factors. However, unlike the porous trabecular strength of bones, the density of the dense type of bones ranges from 0.4 to 0.5 g/cm³, which is still quite high, and the average volumetric density of the femur neck is around 1.0 g/cm³. In addition, the empirical Poisson's ratio of the bone cortex is inherently anisotropic (range 0.15-0.19), which is often not the case in finite-element analyses. Standard computational practices use 0.3 for isotropic and osteoporotic characterizations, as well as scaling ranging between 0.30 and 0.45 for orthotropic characterizations [18]. The Poisson's ratios show high stability with regard to age, bone density, and loading conditions. There are few empirical samples of trabecular bone ratios enough to perform this step-in macro simulation; therefore, the usual Poisson's ratio of 0.3 (corresponding to the usual values in cortical orthotropic bone) is used. Thus, the mean human femoral cortical shear modulus can be well predicted to be 3.3 GPa (minimum-maximum: 2.8–4.0 GPa) [19, 20]. It is also important to note that the shear values in the orthotropic models are in accordance with the general relationships between shear and density, typically expressed as relationships such as

$$G = E/\big(2(1+v)\big) \tag{3}$$

where, E ≈ 17 GPa (Young's modulus) and ν ≈ 0.3 (Poisson's ratio). Tissue-level values can be orders of magnitude greater than 5–6 GPa, as measured by nanoindentation at the lamellar level. The shear modulus of trabecular bone is an order of magnitude lower than that of cortical bone, with such a low apparent modulus of elasticity that this low value has been referred to as hyperelasticity, with a broad range of 0.1 to 1 GPa depending on the bone volume fraction (BV/TV) of 10–25% in trabecular bone. On the other hand, the tissue-level modulus is about 3–4 GPa in trabecular bone, similar to that in cortical bone. In the proximal femur, the sensitivity of shear (G) to density and power-law-type correlations ($G \propto \rho^{\{1.5\text{-}2\}}$) in trabecular regions leads to much of the variability of G in comparison with that in the cortical areas [21]. Orthotropic shear moduli were calculated from ash density for ANSYS simulations, which simulated multi-axial gait loading. Standardized values of the cortical modulus were set to 3.3 GPa, and the trabecular modulus was varied according to its direction, age, and hydration. Ti-6Al-4V alloy (Table 1) was chosen for its excellent biocompatibility, corrosion resistance, and osseointegration. It can resist cyclic gait stresses due to its high fatigue strength and has an elastic modulus (~110 GPa) that can reduce stress shielding in load-bearing implants. Additive manufacturing also has the potential to produce unique, porous scaffolds with ingrowing bone formation. Finally, both materials, bone and implant, were assumed to be isotropic and linear elastic without any regard to plastic material properties.

Table 1. Mechanical and thermal properties of Ti-6Al-4V titanium alloy for biomedical applications

Property	Value
Density	4.429 g/cm³
Young's Modulus	1.112×10^5 MPa (111.2 GPa)
Poisson's Ratio	0.3387
Bulk Modulus	1.149×10^5 MPa (114.9 GPa)
Shear Modulus	41533 MPa (41.533 GPa)
Isotropic Secant Coefficient of Thermal Expansion	8.789×10^{-6} / °C
Tensile Ultimate Strength	918 MPa
Tensile Yield Strength	845.7 MPa

3. THE SIMULATION MODEL DESIGN

SOLIDWORKS models of the femur with appropriately sized subtrochanteric fracture gaps were created. The medullary canal and cortical shell were treated as separate regions to accurately simulate the implant-bone interface using finite element simulations. Four Ti-6Al-4V screws of different parameters were set to have maximum biocritical purchase within the neurovascular margin. They were optimized in a triangulated design that resists axial, bending, and torsional loading and allows controlled interfragmentary motion for secondary bone healing. These were exported to ANSYS in high-fidelity STEP solids following Boolean volume subtraction and coordinate alignment with ANSYS for stable meshing in ANSYS (Figure 1).

Biomechanically, both proximal screws provide stability to the proximal fragment, preventing varus collapse and shear under normal hip loads. They act to direct and transfer joint forces into specific compressive stresses across the fracture gap, encouraging callus formation whilst reducing adverse shear stresses. The two distal screws, on the contrary, hold the construct to the diaphyseal cortex, neutralize forces from the knee, and prevent hardware toggling. This long working length disperses the loading into multiple areas of the diaphysis and significantly minimizes the possibility of screw loosening and/or distal peri-implant fracture. As a group, this is a statically determinate system consisting of four screws, which provides rigid "triangulated" boundary conditions and tightly constrains compressive stability without the possibility of uncontrolled bending.

Figure 1. SOLIDWORKS femur bone design (A) the four screws locations, (B) the main implant bar with its fixture screws, and (C) the complete bone with all parts

4. SIMULATION MODEL MESH

To obtain a high-density unstructured mesh and accurately model the femoral construct, 10-node quadratic tetrahedral elements (SOLID187) were generated in ANSYS 2024 R1. This higher-order discretization is crucial for accurate representations of intricate anatomical and hardware details, such as screw threads and curved cortical surfaces, to achieve reliable stress distributions. The final mesh comprised 2,047,270 nodes and 1,218,317 elements, featuring a mean size of 0.6 mm and a minimum edge length of 3.2917×10^{-3} mm (Figure 2). To reduce the chances of interpolation inaccuracies, curvature and proximity sizing were applied at critical bone-implant interfaces, along with defeaturing algorithms that smooth out minor irregularities on bone surfaces to ensure computational convergence [22]. More specifically, we used localized mesh refinements on the very irregular geometry of the femoral head and neck to accurately model the steep stress gradients under physiological load conditions, while maintaining a smooth transition along the diaphyseal shaft for both accuracy and computational efficiency. Medium-threshold skewness and smoothness metrics were applied to assess the model's overall integrity, yielding a robust framework for advanced fatigue and stress analyses.

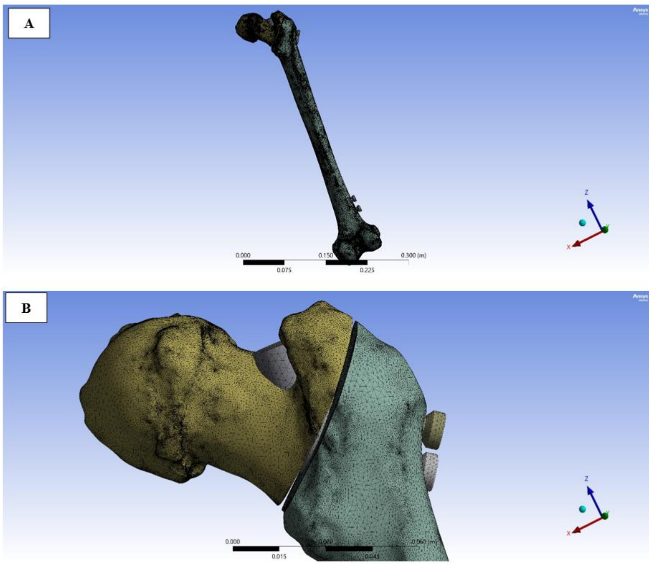

Figure 2. The simulation model mesh: (A) the femur bone mesh with all details, (B) the upper side of the femur bone with the implant and screws mesh

Defeaturing and curvature/proximity sizing were used at key geometries such as fracture interfaces and screw holes to maximize element quality in those critical areas. Targeted high-density refinement (mesh edge length $\geq 3.2917 \times 10^{-3}$ mm) ensured a high level of resolution of steep stress gradients at the highly curved regions of the geometry (the femoral head, neck and distal screw junctions), whilst avoiding increased global mesh densities. Such complicated structures can be modeled precisely, so that interpolation error can be reduced to ensure good stress and strain convergence [22].

5. MESH INDEPENDENCE TEST

The femur fracture model is subjected to a challenging mesh independence test that shows convergence to the numerical solution at extremely small mesh sizes (sub-millimeter). Characteristic element size (between ten million and less than a million degrees of freedom) was varied in the range [0.1 mm, 1.0 mm]; this is detailed in Table 2 and Figure 3, and showed a total deformation plateau in the range [0.6 mm, 1.0 mm]. This plateau validates that global stiffness and load-transfer behaviour of the construct are being captured correctly; while more mesh refinement makes the computation time excessive, it does not make a significant impact on the structural prediction. Therefore, the global element size of 0.6 mm was chosen so the discretization error does not affect the comparative variations and results are exclusively related to the mechanical phenomena.

Although convergence at the global level was achieved by means of deformation on the macro level, localized stress concentrations, such as in the region of screw holes and fracture areas, had to be captured using targeted techniques. As described in Section 4, high-order quadratic tetrahedral elements and extreme localized refinement were used (curvature and proximity sizing towards critical areas such as the distal screw cortex junction). This hybrid solution ensures that peak von Mises stresses can be calculated very accurately, while avoiding the time-consuming mesh of the whole structure with a rather high density.

Table 2. Mesh independence test for the femur fracture element size model

Element Size (mm)	Nodes No.	Elements No.	Deformation (mm)
0.1	61675833	36509010	1.87
0.2	15922257	9418673	1.91
0.3	7308913	4328685	1.84
0.4	4255739	2526081	1.77
0.5	2847581	1692414	1.75
0.6	2047270	1218317	1.72
0.7	1551904	922245	1.72
0.8	1204993	71598	1.72
0.9	992785	589488	1.72
1	825191	489071	1.72

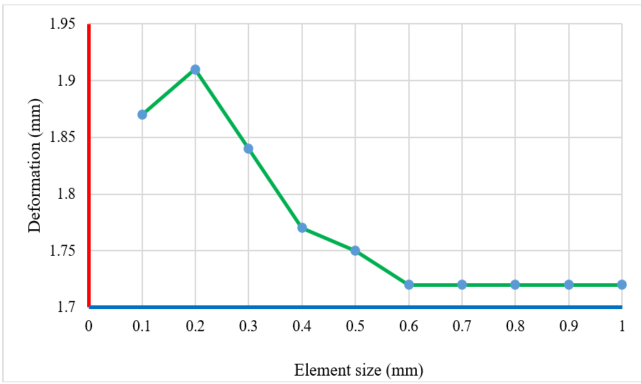

Figure 3. The relation between the mesh element size and the deformation

6. SIMULATION METHODOLOGY AND BOUNDARY CONDITION

The vertical GRF is the axis of the major loads imposed on the femoral implant construct for an 80 kg subject. Global hip joint and ground reaction forces were broken down into vectors across X, Y, and Z directions on the standing, walking, and running models, and the forces were divided for the intramedullary shaft and four locking screws to assess stress and deformation in the different models. A statically determinate load-partitioning methodology was used because of the high numerical noise that would have been generated if used to model the dynamic, non-linear frictional contacts that occur between the 2-million-element mesh. Forces were summed on the proximal screws, the distal screws, and the intramedullary shaft and ensured strict global static equilibrium for all of the loading cases in accordance with existing literature in FEA for free-body equilibrium:

$$\sum F_{global} = F_{shaft} + \sum_{i=1}^{2} F_{prox.i} + \sum_{j=1}^{2} F_{dist,j} \tag{4}$$

To create reproducible fatigue baselines, the loads were applied as nodal forces in the screw coordinate systems. Static structural simulations were performed using the single-step method, ANSYS 2024 R1 software, and a Direct Sparse Solver with a 0.5% convergence tolerance, since the simulations are based on the small-deformation elastic regime and large-deflection effects were not considered. Importantly, the Multi-Point Constraint (MPC) that connects a bone model with an implant model was fully bonded. Physiological interfaces have naturally occurring frictional sliding that buffers stress transmission, but if a simulation of nonlinear friction is conducted on a 2 M element mesh, excessive numerical 'noise' would squelch important information. Using a rigidly bonded statically determinate solution, loads were applied directly to the surface of the cortical bone. In this way, the stress concentrations obtained are conservative, and at the critical distal screws, reliable fatigue assessments can be made.

6.1 Standing case

For the standing baseline case, the ANSYS model represents an 80 kg subject, which corresponds to an approximate vertical hip load under the condition of steady-state. Transverse shear (X/Y) and muscle-driven moments are negligible as quiet standing is a quasi-static, symmetrical posture. Thus, the total resultant load of 784.8 N is simply transferred along the Z-axis as a compressive load along the mechanical axis of the femur. This is then divided into four equal parts to create statically determinate boundary conditions, resulting in 196.2 N of compressive loading per locking screw (Figure 4 and Table 3). Although proximal screws may be able to carry a slightly higher load in reality because of their anatomic location, this equal-share approximation is considered to be a good, mechanically sound baseline for finite element analyses. This setup can help in the basic assessment of the axial stiffness, the distribution of stress, and the safety factor, prior to simulating more complicated multi-axial gait scenarios, by isolating the pure compressive forces and neglecting the dynamic vectors.

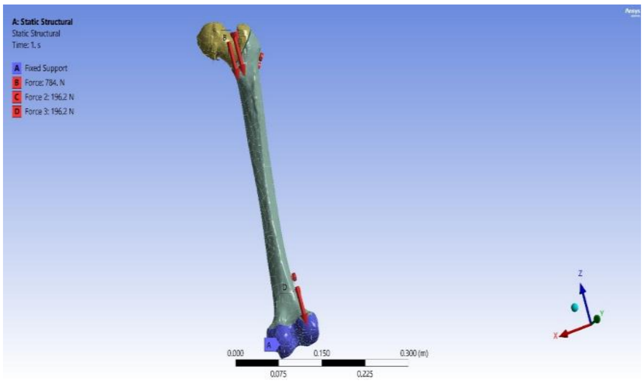

Figure 4. The magnitudes and directions of the acting forces in standing

Table 3. The acting forces and their amounts and directions in the standing case

Component	Z (Vertical/Downward)	X (Forward/Backward)	Y (Lateral/Medial)
Shaft (whole)	-784.8 N	~0	~0
Each Screw (est.)	-196.2 N	~0	~0

6.2 Walking case

Since the walking mechanism was to be accurately simulated for an 80 kg subject (body weight [BW] approx. 784 N) in ANSYS, the joint and ground reaction forces were divided into three axes (X, Y, Z). Validation of in vivo telemetry data showed that this dominant vertical compressive load is at 1–1.5 BW (784–1150 N). Anteroposterior shear (X) was modeled to represent dynamic gait phases at 15% of body weight (BW) to 20% BW (120 N to 160 N), and included negative braking forces during early stance and positive propulsive forces during late stance. Mediolateral shear (Y) was defined as being between 5–10% BW (40–80 N) due to medial and lateral hip shift. These forces (F_X, F_Y, F_Z) were divided up between the intramedullary shaft [23] component and the fixation hardware in order to ensure strict static equilibrium. Reflecting their proximity to the joint load, the proximal screws bore a greater stress proportion (200–400 N in Z, 30–70 N in X, 15–25 N in Y) than the distal screws (150–250 N in Z, 25–55 N in X, 10–20 N in Y). The model can replicate the three-dimensional gait environment with vertical compression and transitional shear, which is physiologically realistic, by applying the above values as localized nodal forces (Figure 5 and Table 4).

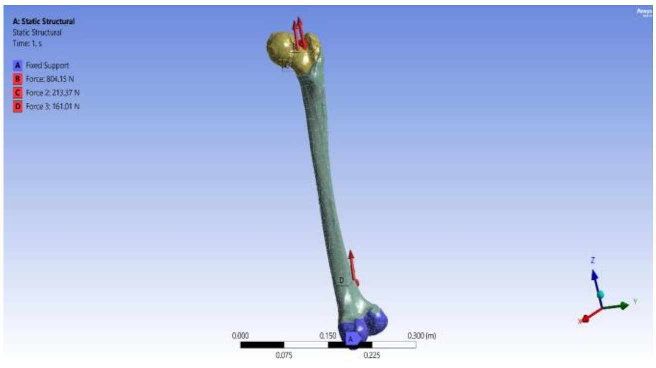

Figure 5. The acting force magnitudes and directions in walking

Placing forces on the implant as it is travelling along the anteroposterior (X-axis), it experiences these forces that are reversed during a gait cycle. The braking phase at initial heel strike is when the ground reaction force is negative and opposing and decelerating forward movement. On the other hand, raising the heel back to stance is the propulsion phase, and will generate a +X-component as the foot is pushed off to help the body propel forward. This mechanical change is vital for efficient means of locomotion. The mediolateral (Y-axis) forces are much smaller than vertical and anteroposterior and dynamically change depending on kinematics. In the traditional anatomical coordinate systems, lateral forces, which push away from the midline, are considered "+" and medial forces, which push towards the midline, are considered. They undergo these directional changes due to contraction acting by forces from the abductor/adductor muscle groups, alignment of the profiles (varus or valgus) as well as differences between individual gaits [24]. Lastly, vertical (Z-axis) loading is usually indicated by coordinates pointing upwards in the biomechanical modelling. Gravity will put a downward force on compression, and finite element analyses will actually depict the opposite ground and structural reaction forces. This means that the 'load' in the Z direction demonstrated in this simulation is the reaction to the body in an upward direction and NOT the gravitational load itself.

Table 4. The acting forces and their directions in the walking case

Component	Z (Upward)	X (Forward/Backward)	Typical Sign
Shaft (whole)	784–1150 N	120–160 N	Z: +, X/Y: ±
Upper Screws	200–400 N	30–70 N	Z: +, X/Y: ±
Lower Screws	150–250 N	25–55 N	Z: +, X/Y: ±

6.3 Running case

Simulated running conditions will produce GRF values of 2.5 to 3.0 times body weight for an 80 kg object. During mid-stance, the dominant compression load (Z-axis) is over 1,962 N and up to 2,353 N. This loading profile is a worst-case load spectrum mechanically, but the fact that it is not allowed to run in the early phase of rehabilitation does not mean that the rest of the load spectrum isn't. It considers the ultimate safety factors of the construct under high-impact accidental overload conditions (for example, severe stumbles or uncoordinated falls). In addition to the vertical load, dynamic multi-axial shear is included. The anteroposterior (X-axis) force is set at 20-25% of body weight (157–196 N) and switched from negative braking to a positive propulsive phase. Mediolateral (Y-axis shear) contributes to 5–10% of body weight (39–78 N), which represents the dynamic oscillation of the pelvis and limbs. The load-path proximity is used to statically partition this global load vector among the four locking screws. Proximal screws bear elevated vertical loads of 500–650 N, alongside 39–49 N in X and 10–19 N in Y [25]. On the other hand, the distal screws can hold 350–525 N vertically with similar shear components [25]. The mentioned loads are then applied in ANSYS software as local nodal loads. This method allows realistic high-impact boundary conditions to be recreated, thus providing good fatigue, stress, and deformation evaluation (Table 5 and Figure 6).

Table 5. The acting forces and their directions in the running case

Component	Z (Down)	X (Forward/Back)	Y (Lateral/Medial)
Shaft (whole)	1,962–2,353 N	157–196 N	39–78 N
Upper Screw	500–650 N	39–49 N	10–19 N
Lower Screw	350–525 N	39–49 N	10–19 N

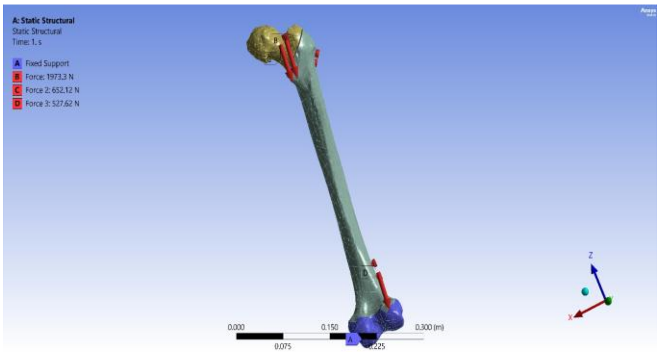

Figure 6. The magnitudes and directions of the acting forces in running

7. RESULTS AND DISCUSSION

7.1 Standing case deformation

In the simulated standing case (Figure 7), the femur-implant construct for an 80 kg person has a maximum total deformation of 0.74 mm at the top of the femur. In the case of the bipedal stance, the compressive hip contact force (784.8 N along the Z-axis) is pure, and there are minimal transverse (X and Y) hip shear forces. This static load is applied equally on the 4 Ti-6Al-4V locking-screws (~196.2 N per screw), and the main mechanical load is applied on the distal femur. As such, this segment has nearly zero deformation and is the stiffest in the construct. Regarding the proximal part of the intramedullary nail spanning the subtrochanteric gap, there will be some compliance allowing a small amount of rigid body translation. Even under a uniaxial compression load, the anatomical lever-arm offset of the femoral head creates a bending moment towards the proximal end of the neck, resulting in the highest displacement occurring in the proximal area of the femoral neck [26]. With a high global stiffness (Ti-6Al-4V modulus approx. 111 GPa), the amount of deformation in the system is sub-millimeter, yielding the 0.6 mm mesh numerically converged and avoiding discretization artefacts. Biomechanically, it acts as a solid column subjected to compression load, with the major principle being to limit interfragmentary micromotions as closely as possible to zero. For clinical purposes, this low amount of deformation reflects a significant safety margin that protects against structural failure, and forms a solid foundation for assessing the increased multi-axial shear loads and stresses in later dynamic simulations of walking and running [27].

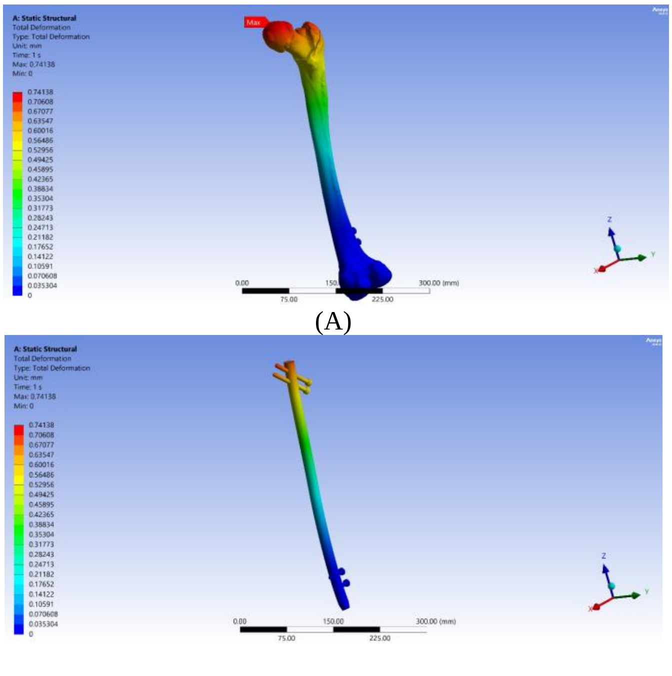

(A)

(B)

Figure 7. Standing case deformation (A) the total femur bone and the implant shaft and fixing screws, (B) the implant shaft and fixing screws deformation

7.2 Walking case deformation

When realistic gait kinematics are added, as shown in Figure 8, the structural response of the femur-implant construct changes from a pure compressed column to a beam in combined load states of axial compression, bending, and mild torsion [28]. This multi-axial loading causes over two times greater structural deformation than static standing, ranging as high as 1.98 mm for Walking Case 1 and 2.95 mm for Walking Case 2, and maximal displacement always occurring at the femoral head. Because of the load transfer path, proximal screws are subjected to significantly greater forces (e.g., 200–400 N in Z) than the more distal screws (150–250 N in Z). In Case 1, the forces are applied vertically and anteroposteriorly, which will have a bending effect on the proximal fragment of the fracture while the distal fragment is held fixed, allowing the compliant subtrochanteric fracture gap to act as a rotational hinge. In case 2, turning the X-component around (simulating the change in the braking/propulsive phase) combined with a slightly higher Z-force results in diaphragmatic bowing of the bone shaft in the opposite direction. A difference of up to 0.97 mm for the significant deformation illustrates the mechanical sensitivity of the construct to the orientation of the X-component in the absence of altering the implant geometry, as it highly increases the bending moment in the cervical construct. The femur-implant system, when loaded during physiological gait, is in a small deformation regime, but in this regime proximal bending causes critical interfragmentary micromotions. This controlled gap displacement optimally stimulates the formation of secondary callus, provided the fatigue limit of the components is not exceeded. However, with increased deformations in L-stance late walking (Case 2) being close to the structural thresholds, especially with osteoporotic bones, postoperatively early level walking should be allowed and excursions in the dynamic phase of walking, such as uneven terrain, should be strongly avoided to prevent high bending moments [29].

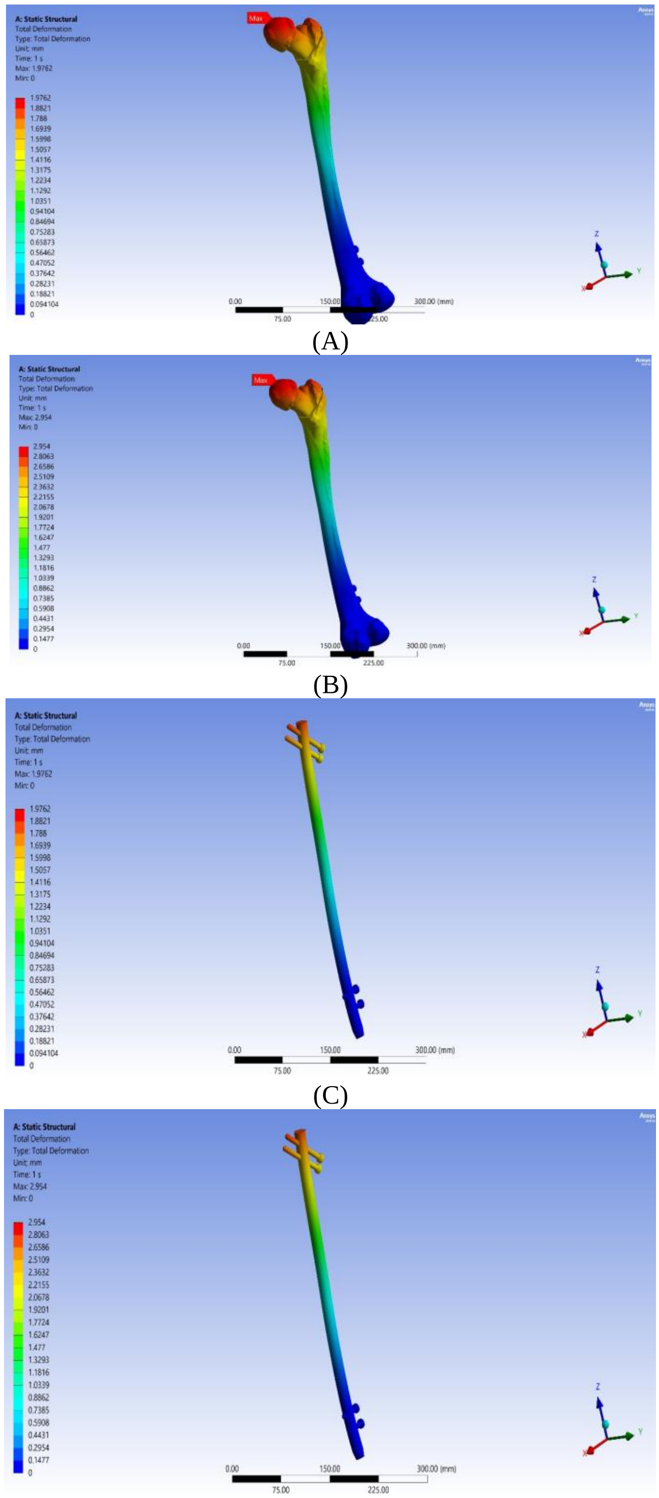

(A)

(B)

(C)

(D)

Figure 8. Walking case deformation (A) and (B) the total femur bone with the implant shaft and fixing screws in cases 1 and 2, (C) and (D) the total femur bone with the implant shaft and fixing screws in cases 1 and 2

7.3 Running cases deformation

The femur-implant construct caused the greatest structural deformations at the femoral head, reaching 3.59 mm (Case 1) and 2.95 mm (Case 2), and proximal constraints were also stable when the running action was simulated (Figure 9). Vertical ground reaction forces of 2.5–3.0 times body weight (1,962–2,353 N) and dynamic anteroposterior shears (157–196 N) and mediolateral shears (39–78 N) occur during running. This is an extremely multiaxial loading, meaning that axial compression is enormous and the intramedullary nail is also bent and twisted. This results in higher bending moments at the subtrochanteric region, which can be beneficial for callus formation, but also takes bone/implant interfaces close to their maximum fatigue limits [30]. Running Case 2: If the direction of anteroposterior shear was reversed (X-component), the deformation peak decreased to 2.95 mm, and the direction of the bowing of the diaphysis was also inverted. This shows that the direction of dynamic shear is the key determinant in the neck bending moments.

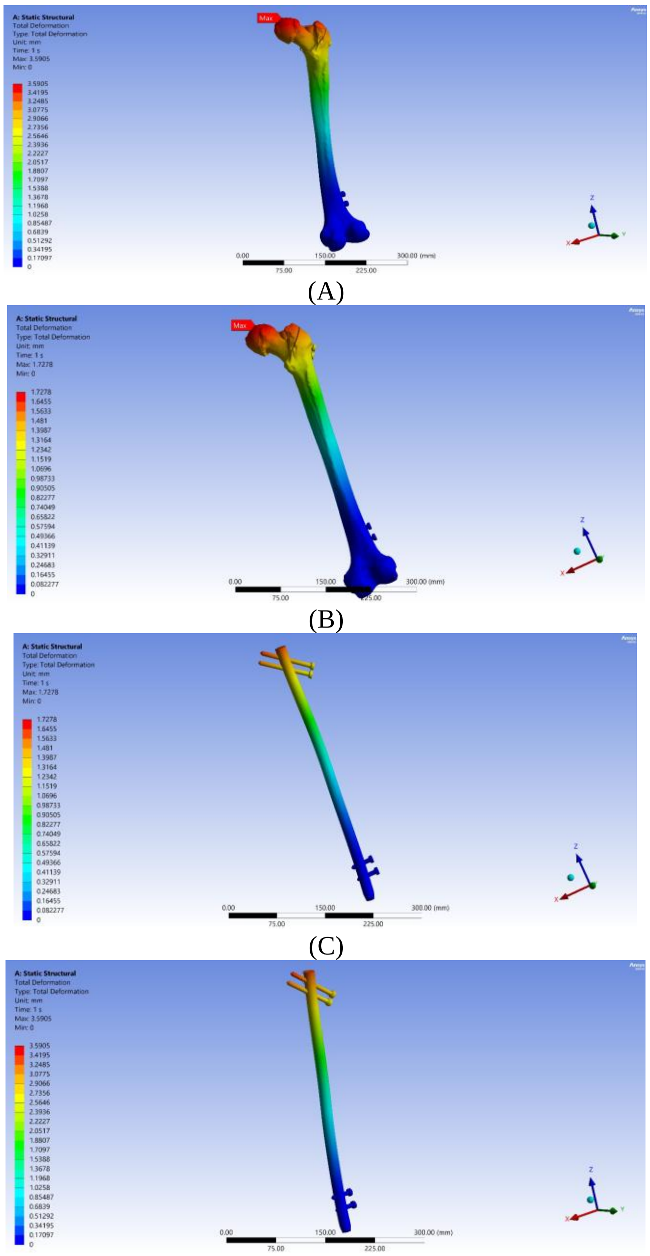

(A) (B) (C) (D)

Figure 9. Running case deformation (A) and (B), the total femur bone with the implant shaft and fixing screws in cases 1 and 2, (C) and (D), the total femur bone with the implant shaft and fixing screws in cases 1 and 2

While in the realm of small-strain elasticity, these loads do not exceed the strengths of the Ti-6Al-4V hardware and cortical bone, the large-strain interfragmentary micromovement significantly increases the risk of screw loosening, implant fatigue, and varus collapse, especially in osteoporotic profiles. Thus, the biomechanical simulations clearly suggest that running and similar high-impact activities be delayed after surgery until good callus formation is radiographically confirmed to ensure that the construct can withstand high-cycle dynamic load without failure.

7.4 The deformation parameter comparisons

7.4.1 Maximum total deformation progressive escalation

With static standing, this approach (Figure 7) yields little deformation (0.74 mm) with pure compression along the vertical axis. The displacement is 1.98 mm (Case 1; 2.7×) and 2.95 mm (Case 2; 4.0×) for walking with anteroposterior shear and its reversal, respectively, demonstrating that the two provide two different levels of amplification of femoral neck bending. In Running Case 2, the deformation value is smaller than Case 1 because of the action of X-component vector shifts at 3.59 mm (4.9×) and 2.95 mm (4.1×), respectively. In short, the goal is to induce this nonlinear structural escalation that relies on a combination of increases in vertical loading (2.5–3.0× rather than 1.0–1.5× body weight) and certain shear directions that maximize loading/bending moments on the cervical spine.

7.4.2 Loading complexity: From uniaxial to multiaxial

Standing also offers the quasi-static baseline, as it represents the situation of pure Z-axis compression (784.8 N) uniformly distributed over the stress points (196.2 N per screw) without transverse shear. Walking is a complex activity of 3D multiaxial loading, involving axial loading of 784-1150 N (1.0-1.5 times BW of Z forces), as well as bending (X forces 120-160 N) and twisting (Y forces 40-80 N), and with alternating gait phases, the X force is inverted to shift the bending plane. During a run, these dynamics are even more extreme, with very high axial compression forces (Z: 1962-2353 N; 2.5-3.0x BW), axial bending and rotation (X: 157-196 N; Y: 39-78 N).

7.4.3 Screw load distribution and implant burden

When standing, 196.2 N of compression is applied to each screw, which is symmetric (equal) load sharing. When walking takes place, asymmetrical loading is applied, and the differences in the magnitude of compression along the screws are as follows: 200–400 N of vertical loading of the proximal screws and 150–250 N in the distal screws, with minor shears in the transverse direction. During running, the load on the proximal joint increases by a factor of 2.5–3.3 to 500–650 N with measurable X and Y shear, while the distal load increases by a factor of 2.5–3.3 to 350–525 N. Such dynamic stresses can significantly increase the risk for interfacial fatigue, hardware loosening, and osteolysis due to micromotion, especially in osteoporotic bone.

7.4.4 Spatial localization and deformation patterns

In all the scenarios evaluated, maximal deformations always occur at the femoral head, which has the longest lever arm and is most unsupported by the distal hardware. When standing, a pattern of smooth, linear displacement fields characteristic of pure axial column behavior. Proximal bending gradient (due to walking): Direct inversion of the bowing direction with switch in the direction of the shear (X-component) imposed. This bending gradient becomes much steeper at the subtrochanteric hinge while running. Finally, it is the direction, NOT the magnitude, of the X-component that is fundamental to the entire deformation topology of the construct.

7.4.5 Biomechanical construct behavior and healing stimulus

How the muscles, joints, and bones react to movements and how to gradually restore normal function. Though these finite element simulations do not attempt to explore dynamic biological healing or diseases such as osteoporosis, they help to create a thorough justification for staged postoperative mobilization: Standing (Baseline Stability): With an axially compressed construct, the system shows very little deformation (0.74 mm) of the construct and minimal interfragmentary micromotion (<0.3 mm). This can create good protection against structural collapse, and has only limited mobility that may not be adequate to promote secondary callus formation optimally.

When transitioning to 3D behaviour–walking, the ideal sub-millimetre micromotion (<1 mm), which is critical for secondary callus remodeling, is generated. Between early-and late-stance phases, however, structural deformation increases by 1.5 times (1.98 mm to 2.95 mm), showing acute sensitivity of the structure to dynamic forces. Early rehabilitation should then focus on the ability to walk level, with no uneven surfaces, and no fast gaits, due to decreased tolerances of the screw-bone interface in osteoporotic bone [31]. Running (High-Impact Overload): Running involves greater-than-usual gap motions in the range of several millimeters, which disturb early fracture healing under the cantilevered beam regime. The Ti-6Al-4V implant can withstand yielding very well, but it causes critical stress concentrations at the distal screw-cortex interface in the surrounding host bone. These findings thus mechanically support the rigid clinical guideline of no high-impact activities until radiographic findings show good callus bridging with bone taking on lots of stiffness [32].

7.5 Standing case stress

However, both the Ti-6Al-4V implant and femoral bone are safely below the allowable stresses of the materials when in quiet standing (Figure 10); however, they differ significantly in their safety margins. The implant functions as an extremely stiff "spine" that can transmit the weight of the body without much deformity. Stresses applied to the intramedullary shaft and screws are mostly under 20 MPa (7–8% of the yield strength of the titanium alloy, 846 MPa), which enables a very high static safety factor (>12).

On the other hand, the global maximum stress of ~61.7 MPa is localized completely within the cortical bone near the lower distal screw, where axial compressive loads start to transfer to the diaphyseal shell. This strain imposes up to 50% of the ultimate capacity of healthy femoral cortical bone, which has a compressive strength of 130–200 MPa. Thus, the limiting mechanical component of the construct is NOT the hardware, but the host cortex. Principally, future design optimizations (such as changing the spacing or diameter of the screws) and clinical protocols should focus on reducing stress concentrations over the lateral cortex, especially in osteoporotic populations, because the risk for yielding of the screws with a load applied remains extremely low.

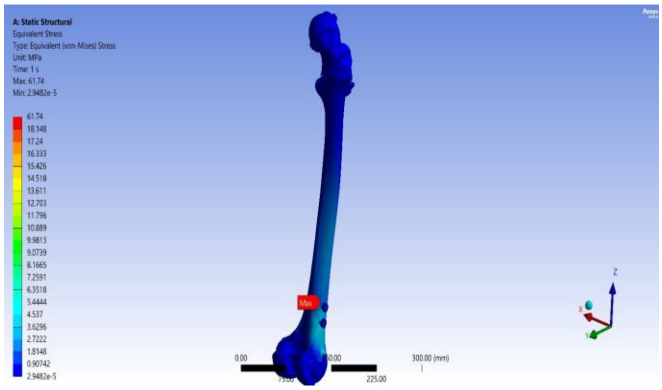

(A)

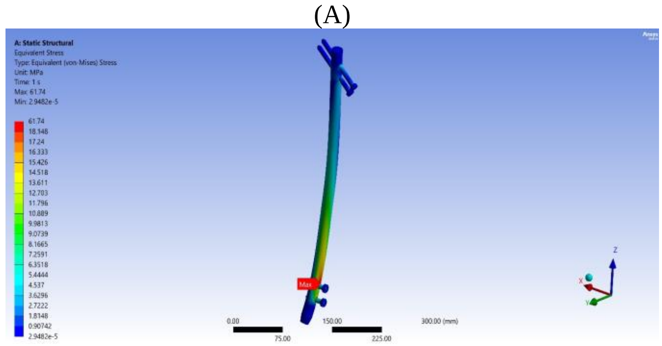

(B)

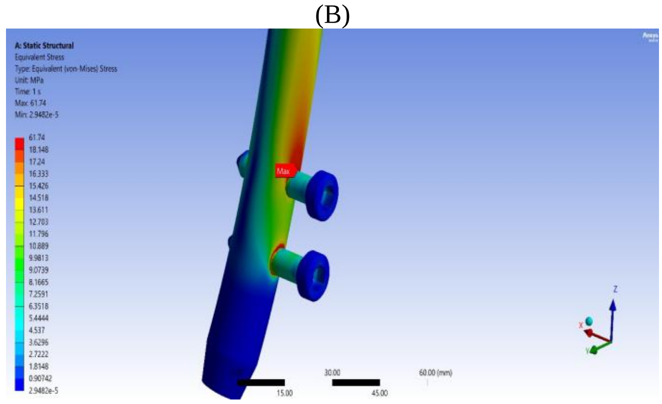

(C)

Figure 10. Stress distribution under standing loading conditions: (A) the femur with the implant shaft and four screws, (B) the implant shaft with four screws, and (C) the location of the maximum stress

7.6 Walking case stress

For Walking Case 1 (Figure 11), the Ti-6Al-4V intramedullary shaft is subjected to a complex loading which consists of a combined axial compression, bending, and light torsional action. This is due to vertical hip contact forces ranging from 784 to 1150 N (1.1–1.5 times body weight), and also due to shear during activity in the anteroposterior (AP) and mediolateral (ML) directions (between 120 and 160 N, and between 40 and 80 N, respectively). In doing so, the resulting general shaft stresses vary between 15–30 MPa, with a highest stress of 80.7 MPa at a location close to the distal screw cluster. Within the implant, the stresses will not exceed 846 MPa, which is below the stress below the implant yielding limit; therefore, the stresses are less than 10% of the capacity of the implant. However, this multiaxial loading causes the construct to behave like a curved loading beam, redistributing stress from diffuse loading along the length of the diaphysis to highly regional distal constructs and the screws of distal fixation. Thus, high loads are borne by the cortical bone around the tension interface of the lower screw, which is close to its load-bearing capacity of 130 to 200 MPa. In biomechanics, the safety margin of the titanium materials against fatigue during normal gait is extremely high. The real weakness is in the host cortical bone at the distal screw interfaces, where great weakness may pose a critical problem, particularly in osteoporotic patients. It is therefore essential to minimize focal cortical stress in clinical strategy and design optimization, such as changes of screw diameter, spacing, or load-sharing mechanisms, and hence avoid "over-engineering" the titanium implant.

When going in the other direction, as simulating propulsion in Walking Case 2 (Figure 12), the load magnitudes are the same (Z: 784–1150 N; X: 120–160 N; Y: 40–80 N); load direction in the Y direction is the same, and load direction in the X direction is the same, but load direction in the Z direction has been reversed. It causes an increase in bending moments and the application of greater shifting and increased stress concentrations in the BON site at the distal fixation site. With this in mind, the global peak von Mises stress was found to be 206 MPa on the lower tensile side of the lower distal screw in the cortical bone, with the Ti-6Al-4V hardware exhibiting safe, low-stress profiles. Under the 206 MPa applied, the titanium alloy is using only ~24% of its yield strength (846 MPa) and 22% of its ultimate strength (918 MPa), providing a still fairly healthy static safety factor against yielding of 4 to 5. In contrast, these localized stresses exceed the normal compressive load-bearing capacity of the human femoral cortex (130–200 MPa). This verifies that the bone-screw junction, and not the implant, is the most important failure point under repeated gait loading. Biomechanically, the switch to a late stance gait dissipates and amplifies as yet another distal bending force without affecting the integrity of the hardware. Thus, the fatigue potential of the titanium hardware under physiological loads must be considered, and future design optimizations, such as adjustments in screw spacing or trajectories, as well as future clinical rehabilitation protocols (e.g., restricted weight-bearing), should be directed toward preserving this vulnerable distal cortical bone [33].

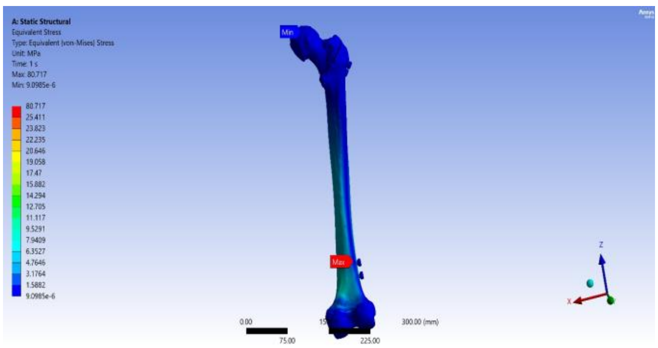
(A)

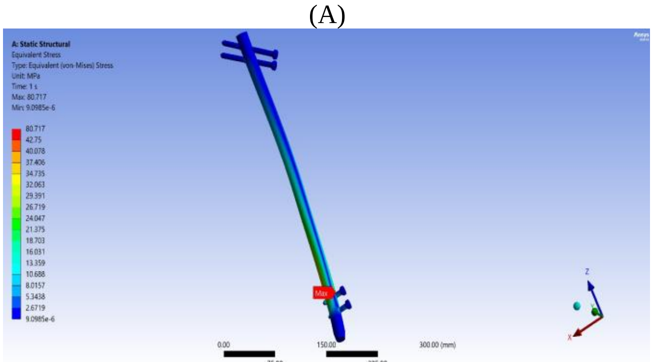
(B)

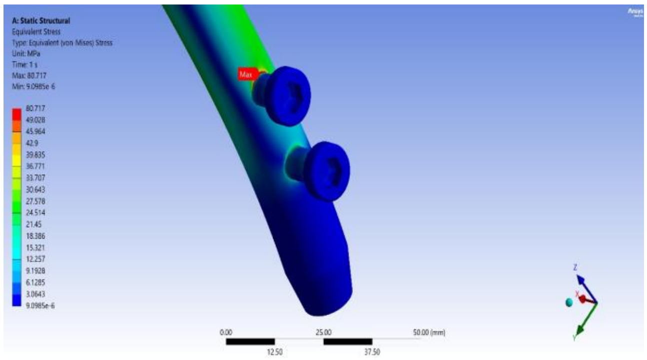
(C)

Figure 11. The walking case (1) stresses (A) the femur bone with the implant shaft and the four screws, (B) the implant shaft and the four screws, and (C) the maximum stress location

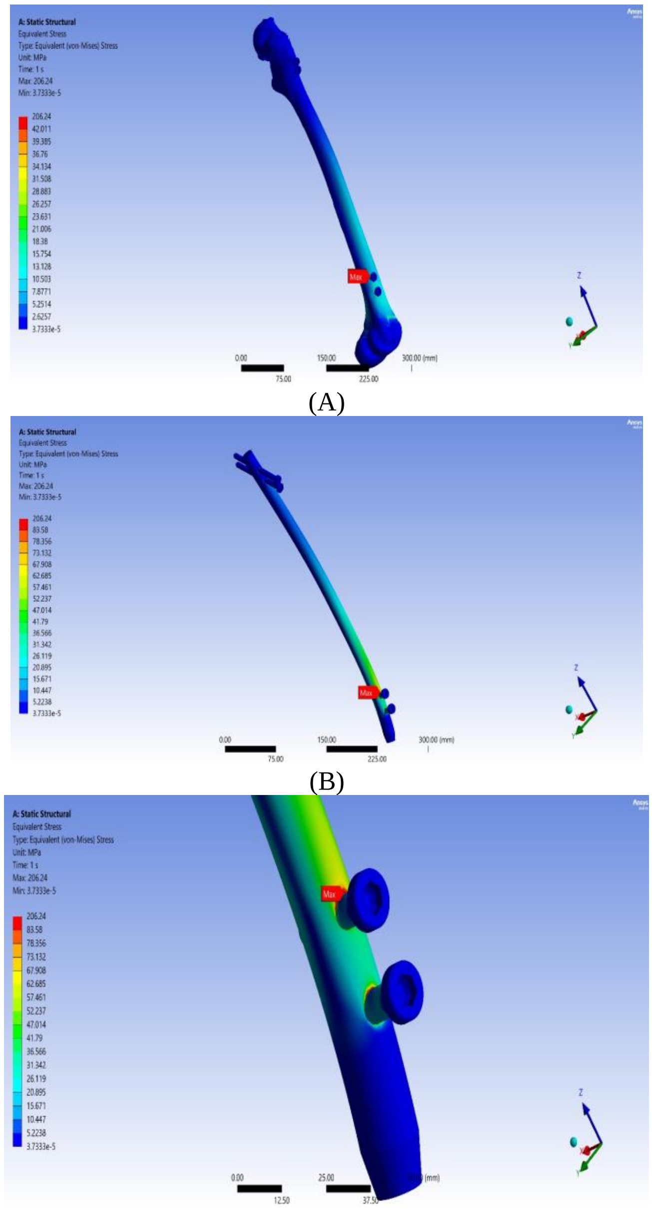
(A)
(B)
(C)

Figure 12. The walking case (2) stress (A) the femur bone with the implant shaft and the four screws, (B) the implant shaft and the four screws, and (C) the maximum stress location

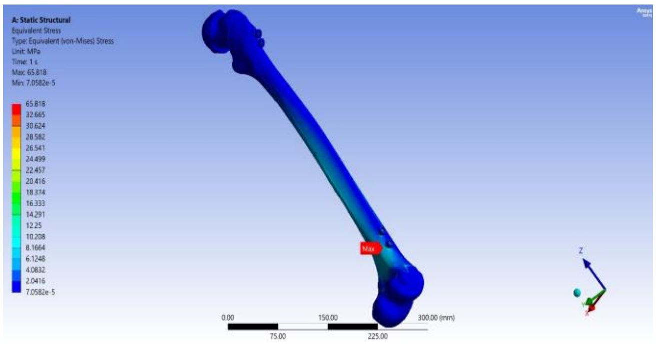

(A)

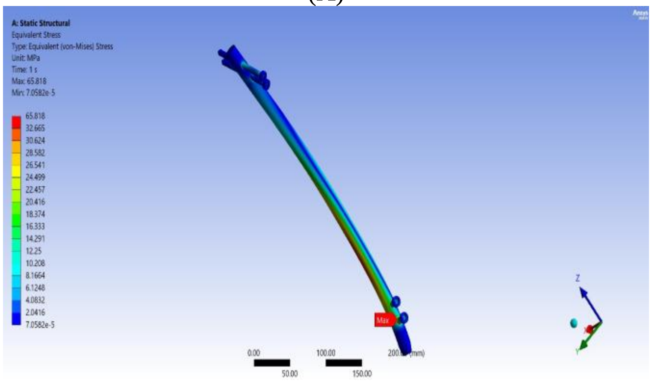

(B)

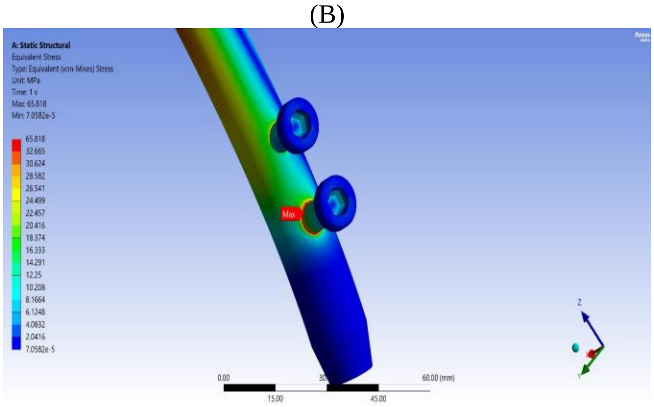

(C)

Figure 13. The running case (1) stress (A) the femur bone with the implant shaft and the four screws, (B) the implant shaft and the four screws, and (C) the maximum stress location

7.7 Running case stress

So, a hip contact force that was 2.5–3.0 times body weight (Z: 1960–2350 N; X: 157–196 N; Y: 39–78 N) caused the construct to act as a clearly bent beam in the Running Case 1 (Figure 13). In the Ti-6Al-4V intramedullary shaft, the bending stresses are continuously 60–70 MPa, which is higher than the stresses of less than 50 MPa experienced during standing and localises at the distal screw cluster. In detail, a maximum local von Mises stress of 65.8 MPa is created in the surrounding elastic zones of the tensile side of the lower distal screw in the elastic area of the cortical bone. The load transfer from the rigid nail into a millimetre-sized cortical annulus is caused by high bending moments, extreme axial loading, and anteroposterior shear. With 65.8 MPa, less than 8% of the yield strength of the titanium (846 MPa) and 7% of the ultimate strength (918 MPa) will be used, giving a considerable safety margin to the hardware, but a significant part of the normal compressive strength of the cortical bone (130–200 MPa) will be utilized. This means that the interface between bone and implant is extremely vulnerable to microdamage and fatigue, and a careful postoperative progression, especially in patients with osteoporosis, is advisable.

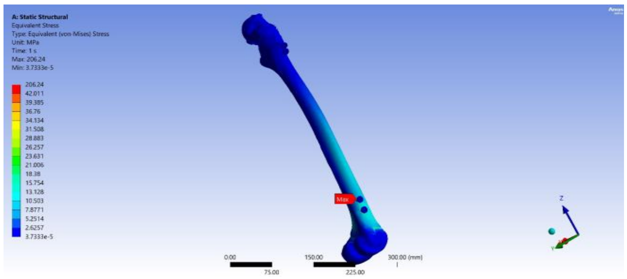

(A)

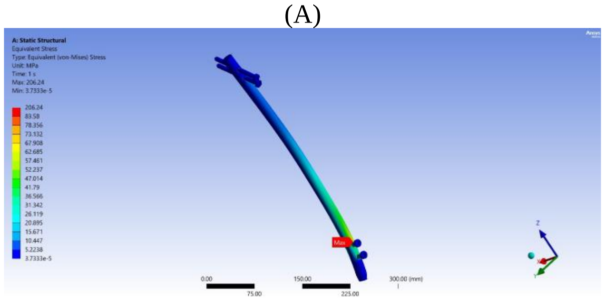

(B)

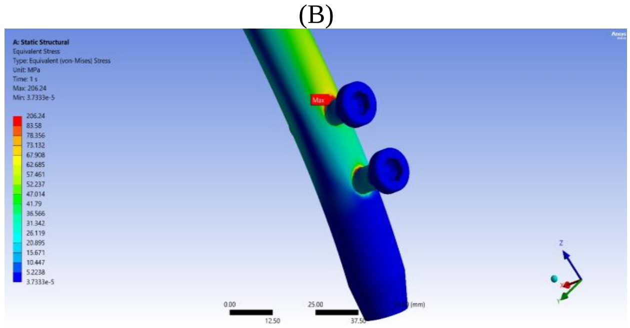

(C)

Figure 14. The running case (2) stress (A) the femur bone with the implant shaft and the four screws, (B) the implant shaft and the four screws, and (C) the maximum stress location

Extreme loads of compression (Z) and 100 N of shear (X) in Running Case 2 (Figure 14) produce a maximum von Mises strain of 291–292 MPa on the bony annulus, around the lower distal screw position, whereas the maximum von Mises stress on the titanium hardware stays in the safe/low stress zone. The yield strength of Ti-6Al-4V is about 292 MPa, which is about 34% of the maximum stress, so it is still safe under static loading. But this concentrated stress was large enough to cause a catastrophic fracture in the femur cortical bone, which is only able to withstand physiologic levels of compression and shear stress. There is a dynamic running-only penalty on the distal fixation zone; the larger cortex at the other locations is mostly below 30 MPa.

These results confirm once again that, in the most challenging gait conditions, the Ti-6Al-4V implant is able to withstand high load, whereas the surrounding cortical bone is loaded to the limits of its structural integrity in high-impact gait activities. As a result, it is essential that rehabilitation programs clearly prioritize safe rehabilitation of running, with the endpoint of the program being a solid gain in callus formation and cortical remodelling. Future optimization should not be directed at strengthening the very strong titanium hardware but perhaps redirecting screw trajectory or designing changes in the compliance or spacing of the hardware to prevent or reduce hazardous distal cortical stresses.

7.8 The stress parameter comparisons

7.8.1 Standing case: Baseline safety and minimal stimulus

Pure vertical compression has a peak stress of 61.7 MPa at the distal screw-cortex interface when standing statically. It only involves approximately 7–8% of the yield strength of the titanium implant, but can still employ up to 50% of the compressive strength of the cortical bone, and make the bone the mechanically limiting component. The minimal interfragmentary motion (0.1–0.3 mm) ensures immediate stability at the risk of losing the important callus healing stimulus.

7.8.2 Walking cases: Transition to physiologic loading

The addition of walking causes multiplanar loading and the mechanics change toward bending of the construct as a beam, resulting in a concentration of stress at the distal cortex. The peak implant stresses were 80.7 MPa (9.5% yield) during Walking Case 1 and 206 MPa (24% yield) during the reversed loading (shear with a larger magnitude) in Case 2. Stresses with this hardware are near or equal to the fatigue strength of the surrounding bone (host cortical bone), which in osteoporotic patients is already low (Safety factor 4–5). However, controlled walking offers optimum sub-millimetre micromotion for secondary callus remodelling (weeks 4–16), and dynamic excursions of gait should be carefully controlled.

7.8.3 Running cases: High stimulus with maximum risk

Both cases have stresses in the cortical bone that are typically dynamic loads with 65.8 MPa (Case 1) and a critical estimate of 291–292 MPa (Case 2), which are higher than the physiological structural limit between 130 and 200 MPa. Long-term construct integrity is governed by the screw-cortex interface, which uses only 32–34% of the ultimate strength of the titanium hardware and still has a healthy yield safety factor of 3. While allowing the maximum stimulation of callus, the amount of interfragmentary motion is dangerous because it increases multiaxial fatigue and screw loosening risks at the bone-implant interface. Thus, unrestricted gait is not recommended after surgery until there is solid radiographic evidence of callus bridging (16–24 weeks postoperatively). Future design optimizations should focus on reducing focal cortical stresses, e.g., using modified screw trajectories or locally compliant features rather than strengthening the material properties of the already over-engineered titanium materials (Table 6).

Table 6. Quantitative comparative analysis of deformation, stress escalation, and structural capacity utilization across physiologic gait conditions

Physiologic Loading Condition	**Max Total Deformation (mm)**	**Deformation % Increase (vs. Standing)**	**Peak Ti-6Al-4V Implant Stress (MPa)**	**Implant % Yield Utilized (Yield = 845.7 MPa)**	**Peak Distal Cortical Bone Stress (MPa)**	**Cortical Stress % Increase (vs. Standing)**	**Cortical Capacity Utilized (Limit ≈ 130–200 MPa)**	**Primary Structural Component**
Standing Case	0.74 mm	Baseline (0%)	50 MPa (45 MPa) 5.3% – 5.9%	61.7 MPa	Baseline (0%)	30.9 – 47.5%	None (Fully safe static equilibrium)	
Walking Case 1	1.98 mm	+167.6%	80.7 MPa	9.5%	80.7 MPa	30.8%	40.4% – 62.1%	Distal Screw–Cortex Interface
Walking Case 2 (Late Stance / Propulsion)	2.95 mm	+298.6%	206 MPa	24.4%	206 MPa	233.9%	103% – 158.5%	Distal Cortical Bone (Fatigue threshold domain)
Running Case 1	3.59 mm	+385.1%	65.8 MPa	+6.6%	32.9% – 50.6%	Distal Screw–Cortex Interface		
Running Case 2	2.95 mm	+298.6% (	292 MPa	34.5%	291–292 MPa	+373.3%	146% – 224.6% (Severe overload limit)	Distal Cortical Bone (High micro-damage risk)

7.8.4 Comparative percentage escalation and structural vulnerability analysis

Multiaxial shear nonlinearly enhanced structure deformation at transition from uniaxial compression. In comparison to the standing baseline (0.74 mm), maximum femoral head displacement had increased by 167.6% (1.98 mm) during early-stance walking, 298.6% (2.95 mm) during late-stance propulsion, and reached a peak of 385.1% (3.59 mm) during high-impact running. Vertical loading determines the compression in the baseplate, whereas anterior-to-posterior forces play a fundamental role in cervical bending moments and interfragmentary micromotions. As detailed in Table 6, these Ti-6Al-4V fixtures did not ever experience structural failure. This was followed by peak stresses from standing (50 MPa) to walking (206 MPa) and running (292 MPa). Even when subjected to extreme running loads, the value of this load only used 34.5% of the yield value of the titanium, leaving a significant static safety factor (2.9-4.1). In addition, standing (<0.3 mm) and walking were proven to be optimal for stimulating sub-millimeter movement for secondary callus stimulation. However, running produced an excess of micromotion, resulting in localized screw-cortex interface stresses that were 233.9% – 373.3% higher than the compressive limit of human cortical bone. Thus, it is the distal cortex, not the Ti implant, that is the mechanically limiting structure, and clinically high-impact activities should be avoided until biologically strong callus consolidation has taken place.

8. VALIDATION

8.1 Implant stresses versus Ti-6Al-4V strength

Peak Ti-6Al-4V stresses are well below yield limits (845–900 MPa; Kurtz,5), and the safety factors are good, even under more aggressive loading states of multiaxial loading. This agrees with Wang et al. [28], who reported that the maximum stresses on the implants did not exceed 50% of the yield stress with 2100 N of axial loading. In a similar manner, Cui et al. [34] noted that, at a load of 700 N, the stresses in nails were sub-yield stress, and this stress gradually decreased as the healing bone took on the load. In conclusion, these combined results confirm that the mechanics itself is also very over-engineered and does not limit the safety of the construct under physiological gait.

8.2 Load levels and boundary conditions

Our applied loading scheme (standing approx. 784 N, walking 784-1150 N, running 1960-2350 N; transverse loading shear X approx. 15-25% BW, Y approx. 5-10% BW) is well substantiated by previously developed finite element models of subtrochanteric nails [35]. Existing literature also uses 700–1200 N for baseline gait, and up to 2500 N for high-demand activities, and includes similar vectors for multiaxial activities [36]. As in these previous models, the increase in the peak loads mainly increases bending of the proximal shaft segments.

8.3 Distal screw and cortical bone stress concentration

There is critical peak stress localization at the distal locking screws between a stand-to-run loading. Model results show that the stresses in the adjacent cortical material exceed yield limits while the implant itself does not exceed yield. This confirms the observations of Kwak et al. [36] of von Mises stresses in the distal part of the 180–230 MPa at 2000 N, and similarly, analogous FEA [37] has reported stresses of more than 200 MPa at 2500 N loading. Our main conclusions based on these collective findings are that the host cortical bone and not the strong titanium hardware is the mechanically limiting structure for high-impact running.

8.4 Construct stiffness, micromotion, and rehabilitation rationale

Although walking causes optimal sub-millimeter micromotion for secondary callus formation, standing gives immediate stability but is not enough to provide a biological healing stimulus. On the other hand, high-impact running creates an excessive amount of interfragmentary movement and overload for the bone screws, especially in osteoporotic patients. Mechanically, this is in alignment with Martínez-Martínez et al. [11], who showed that up to 3× body weight produces strains corresponding to delay in union, while early ambulation can be done without problems when the fixation is titanium. These additional simulations confirm that they threaten interface integrity before sufficient biological remodeling and provide strict validation of a mimicking, progressive rehabilitation protocol.

8.5 Choice of fixation and allowed activity level

Intramedullary fixation allows for repeatable, protected early and progressive rehabilitation that is both safe and more intense than can be safely achieved with the use of extramedullary plate systems; however, biological limitations such as bone quality and integrity of soft-tissue structures will impact the physiological limits to early and progressive rehabilitation. These walking simulations by others have been confirmed by Mu et al. [38], who showed that intramedullary devices can withstand progressive daily loading earlier than extramedullary devices. This helps guide our proposed rehabilitation protocol and reminds us of how important it is to track the distal screws as patients move toward running. More importantly, we quantitatively validate our finite element framework with well-established experimental and cadaveric benchmarks in Table 7. Even with high-density 3D gait vectors and converged tetrahedral meshing, such an "in silico" method has limitations. This particular four-screw construct has not yet been physically tested, but our computational results are in good agreement with previous validated biomechanical models [28, 35-37]. Therefore, these derived stress magnitudes can only be used for comparative in vivo biomechanical indices.

Table 7. Comparison of simulated implant stress, cortical stress, and micromotion outputs with established biomechanical references

Biomechanical Parameter	Present Study Output	Published Benchmark Data	Reference and Methodology	Validation Correlation
Peak Implant Stress (Walking / Axial)	80.7 – 206 MPa (Safety Factor 4–5 against yield)	~50% of Ti-6Al-4V yield stress (Safety Factor 1.5–2.0 under 2100 N)	Wang et al. [28] (Validated FEA of PFBN/PFNA); Cui et al. [34]	Confirms Ti-6Al-4V implant acts as an overdesigned, fatigue-resistant carrier.
Distal Screw Cortex Stress (High Load / Running)	206 MPa (Walking) to 291–292 MPa (Running) at distal screw entry	180 – 230 MPa (at 2000 N load); >200 MPa (at 2500 N cyclic load)	Kwak et al. [36] (Subtrochanteric FEA); Cho et al. [37] (Cyclic load experiment & FEA)	Confirms distal cortical bone—not titanium—is the primary site for fatigue failure and micro-damage.

Interfragmentary Micromotion	~0.1–0.3 mm (Standing); Sub-millimeter (Walking)	Controlled sub-millimeter motion promotes secondary callus bridging without delayed union	Martínez-Martínez et al. [11] (Patient-specific mechanobiological healing model)	Validates that construct stiffness appropriately maps onto physiological healing timelines.

8.6 Limitations of the study

The bone was assumed to be a linear elastic, homogeneous and isotropic/orthotropic material [16, 17, 19, 20]. Although it is used for measuring primary stability, this ignores the fact that bone is anisotropic, viscoelastic, and heterogeneous. The resulting maximal stress values in the distal portion of the screw cortex (walk, 206 MPa; run, 292 MPa) are thus worst-case scenarios; the actual stresses during loading are lower due to the diffusive effect of living bone, using post-yield plasticity and anisotropic stiffness behavior. However, the use of the yield strength of the Ti-6Al-4V implant (aimed at less than 24% of the implant tensile strength) strengthens our main conclusion that the acceptance of the host cortex, not the implant, has not allowed it to fail in high-impact loadings. Future work will combine these models with the mapping of CT density and the application of elastoplastic laws.

Other boundary conditions such as active muscle contraction (e.g., gluteus medius or iliopsoas) were not considered. Physiologically, the muscles are developed as a tension band for the lateral bending moments through the femoral shaft [31]. On purpose, excluding them causes the construct to absorb undamped bending, setting a fixed maximum stress limit of 291–292 MPa. This is proof of the implant's reliability in vivo because it was able to withstand the high extremes of these unmitigated mechanical conditions while maintaining high safety factors. Validation to be conducted in the future will include the use of a muscle-loading profile to validate the physio against the test.

The research paper used a manual load-partitioning scheme instead of an automated, non-linear contact scheme. To eliminate peak forces that occur with frictional damping in localized macro slip, these forces were applied directly at the screw-cortex interfaces without damping by localized frictional slip. This simplification will produce a worst-case conservative stress concentration. These extreme loading conditions (static safety factor ≥3-4) were easily borne by the Ti-6Al-4V hardware, adding further proof of the over-structuring of the material and supporting our clinical advice to restrict high-impact activities until radiographic proof of callus bridging can be achieved. This in silico model looks at mechanical/primary stability and does not consider dynamic biological healing. A void was used to approximate the fracture space and the progressive mechanical stiffening of granulation tissue and the formation of callus to resolve the load from the implant. Also, patient-specific factors, such as osteoporosis, weren't taken into account, but it's possible that lower bone mineral density would increase the focal distal stresses even more and raise the risk of varus collapse. Thus, the rehabilitation time frames proposed herein are only tentative biomechanical baselines that need to be properly confirmed radiologically and biologically prior to use as appliers.

9. CONCLUSIONS

This FEA showed that the provided fixation of the subtrochanteric fractures stabilized by a Ti-6Al-4V intramedullary nail locked with four screws was strong under all physiological loads. The main findings are presented below:

•The model was represented with an anatomy from the CT scans, and stress and deformation results were calculated through 0.6 mm tetrahedra with the correct application of three-dimensional forces from the standing (784.8 N), walking (784–1150 N), and running (1962 – 2353 N) conditions.

•The kinematic behavior was also studied, and the CONSTRUCT stiffness parameters were retained with a progressive increase in the maximum femoral head deformation in a non-linear fashion from standing (0.69 mm) to walking (1.98 – 2.95 mm) and running (2.95 – 3.59 mm). This is due to a change in mechanical loading from axial compression to cantilever bending as activity increases.

•To facilitate the formation of secondary callus, the micromotion & healing stimulus developed as follows: cleft-like stability during standing (0.1-0.3 mm) to optimum sub-millimeter freedom of movement during walking. On the other hand, running caused the gap motion to be too high, which was possibly harmful.

•The stresses in the implants at all instances were well below the Ti-6Al-4V yield stress (845.7 MPa). Even when running under extreme loads, the maximum hardness stresses used only 24% of the yield strength, allowing for safety factors of static orders of three to four.

•The actual mechanical end point has nothing to do with the strength (or weakness) of the titanium hardware, but rather the malleability of the surrounding host cortical bone (cortical vulnerability). Distal cortical stresses were progressively increased (walking) to 206 MPa and (running) to 292 MPa compared to 61.7 MPa when standing and were critical to the conventional distal cortical failure limits under the increased stresses during walking and running activities.

•During dynamic gaits, there were large asymmetric load distributions on the distal fixation to note, specifically multiaxial shear loadings, implying that this is the most important region to watch clinically and tweak designs for further improvements.

•The concept's load transfer has changed from pure diaphyseal compression when standing statically to a predominantly bending-dominated focal stress concentration at the distal screw-cortex interface during active gait.

These findings mechanistically validate staged postoperative loading that is called Rehabilitation Protocols. With controlled walking, the healing stimuli remain optimum, but with extreme interface stress, a high-impact walking protocol should be avoided until a firm radiograph is obtained.

With a functionally over-engineered Ti-6Al-4V implant for physiological loads, certain design modifications should not increase the strength of the implant. Rather, optimum adjustment of screw angulation, spacing, or flexibility must be used to reduce stresses at the distal cortex and maintain the integrity of the host bone.

REFERENCES

[1] Tucker, S.M., Wee, H., Fox, E., Reid, J.S., Lewis, G.S.

(2019). Parametric finite element analysis of intramedullary nail fixation of proximal femur fractures. Journal of Orthopaedic Research, 37(11): 2358-2366. https://doi.org/10.1002/jor.24401

[2] Ye, K., Wang, Y., Dong, Y., et al. (2025). The influence of proximal femur CT value on stress distribution and stability in intertrochanteric fracture after PFNA fixation: A finite element analysis. BMC Musculoskeletal Disorders, 26(1): 747. https://doi.org/10.1186/s12891-025-08982-5

[3] Lowen, G.B., Garrett, K.A., Moore-Lotridge, S.N., et al. (2022). Effect of intramedullary nailing patterns on interfragmentary strain in a mouse femur fracture: A parametric finite element analysis. Journal of Biomechanical Engineering, 144(5): 051007. https://doi.org/10.1115/1.4053085

[4] Yang, Y., Wu, D., Cheng, X., et al. (2025). Biomechanical evaluation of the triangular support structure of the proximal femoral bionic nail compared to conventional long intramedullary nails for subtrochanteric fractures. Frontiers in Bioengineering and Biotechnology, 13: 1579842. https://doi.org/10.3389/fbioe.2025.1579842

[5] Fu, G., Zhong, G., Yang, Z., Cheng, S., Ma, L., Zhang, Y. (2022). Two cannulated screws provide sufficient biomechanical strength for prophylactic fixation in adult patients with an aggressive benign femoral neck lesion. Frontiers in Bioengineering and Biotechnology, 10: 891338. https://doi.org/10.3389/fbioe.2022.891338

[6] Hidaka, R., Matsuda, K., Nakamura, M., Nakamura, S., Kawano, H. (2022). Optimal combined anteversion range for obtaining a wider range of motion without prosthetic impingement after total hip arthroplasty: A three-dimensional analysis study. Journal of Orthopaedic Surgery and Research, 17(1): 226. https://doi.org/10.1186/s13018-022-03112-6

[7] Wang, H.R., Li, J., Zhang, L.F., et al. (2024). Biomechanical analysis of fixation strength at different nailing angles for femoral neck fracture with insufficient reduction. Computer Methods in Biomechanics and Biomedical Engineering, 27(13): 1949-1959. https://doi.org/10.1080/10255842.2023.2265010

[8] Kishore, R., Alam, M., Thahseen, N., Cm, B., Vellingiri, K., Rajendran Sr, R.K. (2025). Retrograde intramedullary nailing for distal femur fractures: A prospective study of functional outcomes, complications, and union rates. Cureus, 17(4): e82139. https://doi.org/10.7759/cureus.82139

[9] Trompeter, A., Christen, A., Gerber, C., Hofstaetter, B., Wipf, F., Lowe, J. (2025). The influence of “kickstand” screws on the mechanical performance of a lateral distal femoral plate: A finite element analysis. Bone & Joint Research, 14(8): 713. https://doi.org/10.1302/2046-3758.148.BJR-2024-0479.R1

[10] Xu, Z., Li, Y., Tian, S., Xu, X., Zhou, H., Yang, M. (2025). Preliminary exploration of finite element biomechanical preoperative planning for complex tibial plateau fractures. Scientific Reports, 15(1): 15913. https://doi.org/10.1038/s41598-025-01085-0

[11] Martínez-Martínez, A., Nadal, E., Bonete, D., Allix, O., Ródenas, J.J. (2024). Patient-specific numerical simulation of the bone healing process including implant materials and gait conditions. Finite Elements in Analysis and Design, 236: 104153. https://doi.org/10.1016/j.finel.2024.104153

[12] Bavil, A.Y., Eghan-Acquah, E., Dastgerdi, A.K., et al. (2025). Simulated effects of surgical corrections on bone-implant micromotion and implant stresses in paediatric proximal femoral osteotomy. Computers in Biology and Medicine, 185: 109544. https://doi.org/10.1016/j.compbiomed.2024.109544

[13] Bavil, A.Y., Eghan-Acquah, E., Barrett, et al. (2026). Selected postoperative neck-shaft angle in proximal femoral osteotomy can affect the bone healing: A finite element study. IRBM, 47(1): 100919. https://doi.org/10.1016/j.irbm.2025.100919

[14] Ülker, A., Satılmış, A.B., Uzunay, Z., et al. (2025). Biomechanical comparison of the new-generation implant designed for the fixation of patella fractures with the tension band method. Medicina, 61(6): 952. https://doi.org/10.3390/medicina61060952

[15] Eghan-Acquah, E., Bavil, A.Y., Bade, D., et al. (2024). Enhancing biomechanical outcomes in proximal femoral osteotomy through optimised blade plate sizing: A neuromusculoskeletal-informed finite element analysis. Computer Methods and Programs in Biomedicine, 257: 108480. https://doi.org/10.1016/j.cmpb.2024.108480

[16] Wang, Y., Yang, L., Li, C., Sun, H. (2022). The biomechanical properties of cement-augmented pedicle screws for osteoporotic spines. Global Spine Journal, 12(2): 323-332. https://doi.org/10.1177/2192568220987214

[17] Fan, J., Xu, X., Zhou, F. (2022). The lateral femoral wall thickness on the risk of post-operative lateral wall fracture in intertrochanteric fracture after DHS fixation: A finite element analysis. Injury, 53(2): 346-352. https://doi.org/10.1016/j.injury.2021.11.015

[18] Morgan, E.F., Unnikrisnan, G.U., Hussein, A.I. (2018). Bone mechanical properties in healthy and diseased states. Annual Review of Biomedical Engineering, 20(1): 119-143. https://doi.org/10.1146/annurev-bioeng-062117-121139

[19] Sun, X., Wu, W., Zhang, R., et al. (2022). Mechanical response and in-situ deformation mechanism of cortical bone materials under combined compression and torsion loads. Plos One, 17(7): e0271301. https://doi.org/10.1371/journal.pone.0271301

[20] Baleani, M., Erani, P., Acciaioli, A., Schileo, E. (2024). Tensile yield strain of human cortical bone from the femoral diaphysis is constant among healthy adults and across the anatomical quadrants. Bioengineering, 11(4): 395. https://doi.org/10.3390/bioengineering11040395

[21] Feng, C., Zhang, K., Zhan, S., Gan, Y., Xiang, X., Niu, W. (2024). Mechanical impact of regional structural deterioration and tissue-level compensation on proximal femur trabecular bone. Frontiers in Bioengineering and Biotechnology, 12: 1448708. https://doi.org/10.3389/fbioe.2024.1448708

[22] Joshi, A., Karande K., Gunaki, R. (2025). Finite element analysis of proximal femur fractures: Evaluating fatigue performance and factor of safety of DHS screw fixation. Biomedical and Pharmacology Journal, 18(3): 2277-2289. https://doi.org/10.13005/bpj/3254

[23] Ye, K., Xing, Y., Zou, D., et al. (2023). Positive correlation between the proximal femur hounsfield units from routine CT and DXA results. Journal of Orthopaedic Research, 41(12): 2648-2656. https://doi.org/10.1002/jor.25630

[24] Ye, K.F., Xing, Y., Sun, C., et al. (2020). Loss of the posteromedial support: A risk factor for implant failure after fixation of AO 31-A2 intertrochanteric fractures. Chinese Medical Journal, 133(1): 41-48. https://doi.org/10.1097/CM9.0000000000000587

[25] Puram, C., Pradhan, C., Patil, A., Sodhai, V., Sancheti, P., Shyam, A. (2017). Outcomes of dynamic hip screw augmented with trochanteric wiring for treatment of unstable type A2 intertrochanteric femur fractures. Injury, 48: S72-S77. https://doi.org/10.1016/S0020-1383(17)30498-9

[26] Taylor, M., Viceconti, M., Bhattacharya, P., Li, X. (2021). Finite element analysis informed variable selection for femoral fracture risk prediction. Journal of the Mechanical Behavior of Biomedical Materials, 118: 104434. https://doi.org/10.1016/j.jmbbm.2021.104434

[27] Nie, B., Chen, X., Li, J., Wu, D., Liu, Q. (2017). The medial femoral wall can play a more important role in unstable intertrochanteric fractures compared with lateral femoral wall: A biomechanical study. Journal of Orthopaedic Surgery and Research, 12(1): 197. https://doi.org/10.1186/s13018-017-0673-1

[28] Wang, Y., Chen, W., Zhang, L., et al. (2022). Finite element analysis of proximal femur bionic nail (PFBN) compared with proximal femoral nail antirotation and InterTan in treatment of intertrochanteric fractures. Orthopaedic Surgery, 14(9): 2245-2255. https://doi.org/10.1111/os.13247

[29] Huang, H., Feng, Z., Wang, W., Yang, C., Liao, J., Ouyang, J. (2021). Finite element analysis of femoral neck fracture treated with bidirectional compression-limited sliding screw. Medical Science Monitor: International Medical Journal of Experimental and Clinical Research, 27: e929163-1-e929163-8. https://doi.org/10.12659/MSM.929163

[30] Noda, M., Nakamura, Y., Adachi, K., Saegusa, Y., Takahashi, M. (2018). Dynamic finite element analysis of implants for femoral neck fractures simulating walking. Journal of Orthopaedic Surgery, 26(2): 2309499018777899. https://doi.org/10.1177/2309499018777899

[31] Edwards, W.B., Miller, R.H., Derrick, T.R. (2016). Femoral strain during walking predicted with muscle forces from static and dynamic optimization. Journal of Biomechanics, 49(7): 1206-1213. https://doi.org/10.1016/j.jbiomech.2016.03.007

[32] Ahmed, U., Ahmad, U., Zaheer, M., Sadaqat, A., Khalid, Z. (2021). Comparison of outcome with retrograde nailing versus locked compressive plating in the treatment of extra articular supracondylar femur fractures. Methodology, 15(12): 3410-3412. https://doi.org/10.53350/pjmhs2115123410

[33] Yadav, C.B., Rajak, A., Shrestha, B.P., et al. (2020). Functional outcome of retrograde nailing versus locked plating of extra-articular distal femoral fractures in adults: A randomized controlled trial. Journal of Kathmandu Medical College, 9(3): 122-129. https://doi.org/10.3126/jkmc.v9i3.36404

[34] Cui, Y., Xing, W., Pan, Z., et al. (2020). Characterization of novel intramedullary nailing method for treating femoral shaft fracture through finite element analysis. Experimental and Therapeutic Medicine, 20(2): 748-753. https://doi.org/10.3892/etm.2020.8763

[35] Je, D.Y., Kim, J.W., Lee, S.J., Kim, C.H. (2024). What is the optimal nail length to treat osteoporotic subtrochanteric fractures? A finite element analysis. Clinics in Orthopedic Surgery, 16(3): 363. https://doi.org/10.4055/cios23234

[36] Kwak, D.K., Bang, S.H., Kim, W.H., Lee, S.J., Lee, S., Yoo, J.H. (2021). Biomechanics of subtrochanteric fracture fixation using short cephalomedullary nails: A finite element analysis. Plos One, 16(7): e0253862. https://doi.org/10.1371/journal.pone.0253862

[37] Cho, H.M., Choi, S.M., Park, J.Y., Lee, Y., Bae, J.H. (2022). A finite element analysis and cyclic load experiment on an additional transcortical-type hole formed around the proximal femoral nail system's distal locking screw. BMC Musculoskeletal Disorders, 23(1): 92. https://doi.org/10.1186/s12891-022-05006-4

[38] Mu, J.X., Xiang, S.Y., Ma, Q.Y., Gu, H.L. (2021). Selection of internal fixation method for femoral intertrochanteric fractures using a finite element method. World Journal of Clinical Cases, 9(22): 6343-6356. https://doi.org/10.12998/wjcc.v9.i22.6343